Supplementary Information

Lattice engineering mediated fast decay in $Li_2HfF_6:Mn^{4+}$ with dual-excitation-band responsive differential emission for fingerprinting, anti-counterfeiting, and optical signal transmission

Ping Yue,[a] Ke Chang,*[a] Zhiyu Qin,[a] Wanjie Ding,[a] Yue Zhao,[a] Langping Dong,[a] Yufeng Liu,[a] Haijie Chen,*[b] Yongzheng Fang *[a] and Jingshan Hou *[a]

[a]Faculty of Materials Technology, Shanghai Institute of Technology, Shanghai, 201418, China.

Email: chang_ke@sjtu.edu.cn; fangyongzheng@sit.edu.cn; houjingshan@sit.edu.cn.

[b]State Key Laboratory of Advanced Fiber Materials, College of Materials Science and Engineering, Donghua University, Shanghai, 201620, China.

Email: haijie.chen@dhu.edu.cn.

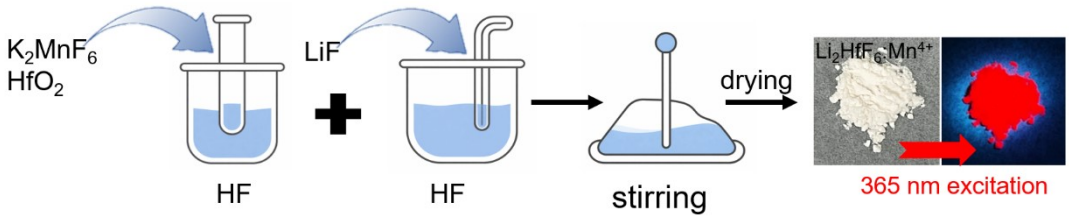

Figure S1. Schematic diagram of the synthesis of LHFM red phosphor via co-precipitation method.

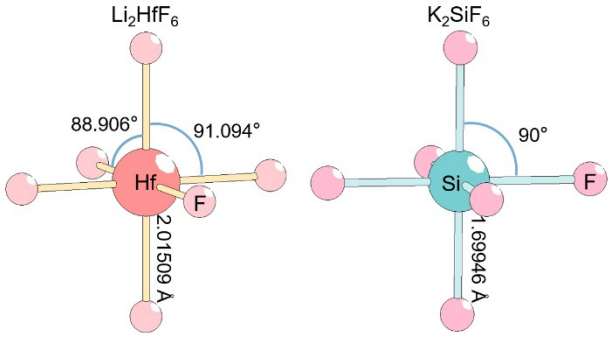

Figure S2. Ball-and-stick models of the HfF_6 and SiF_6 octahedra in Li_2HfF_6 (left) and K_2SiF_6 (right).

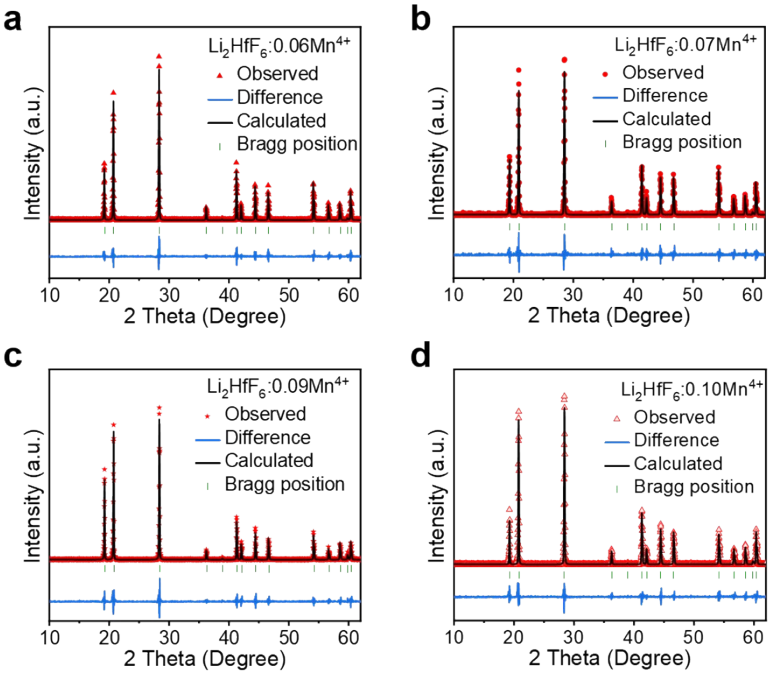

Figure S3. Rietveld refinement result of Li_2HfF_6:xMn^{4+}(x = 0.06, 0.07, 0.09. 0.10).

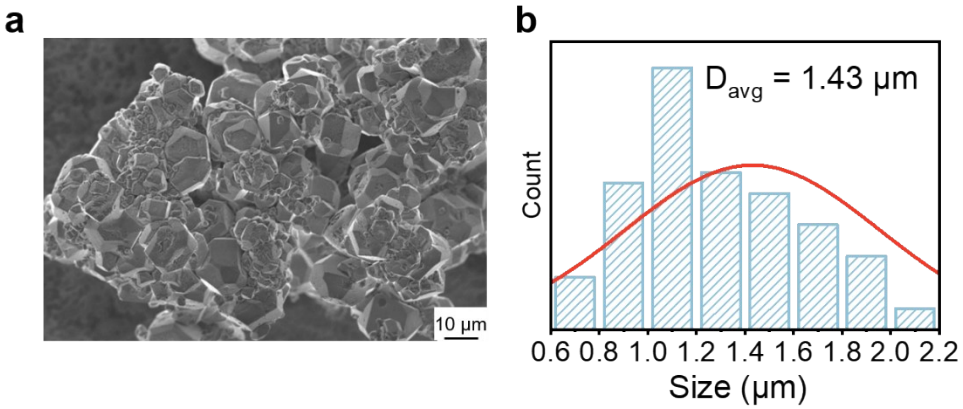

Figure S4. (a) SEM image and (b) Particle size distribution histogram of Li_2HfF_6:0.08Mn^{4+} samples.

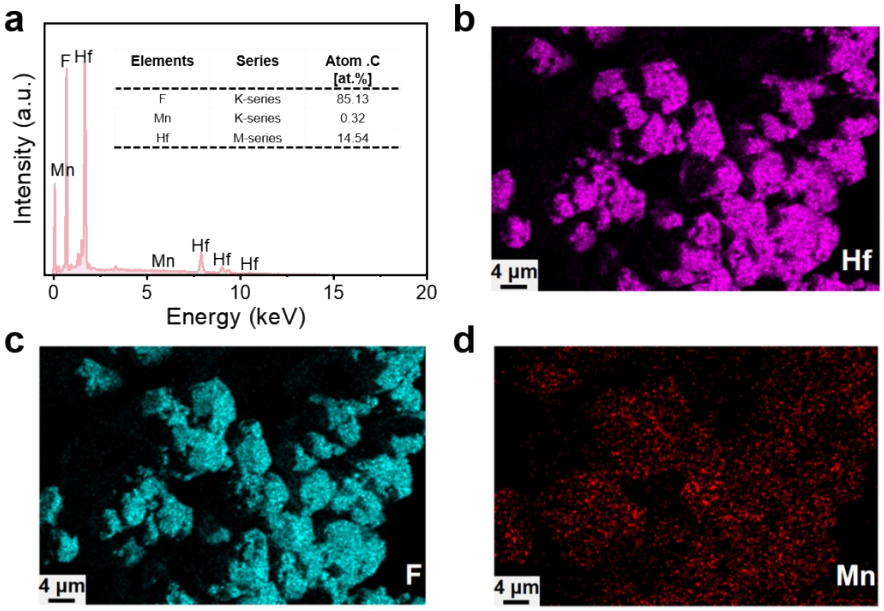

Figure S5. (a) EDS characterization of Li_2HfF_6:0.08Mn^{4+} powder. (b-d) SEM elemental mapping.

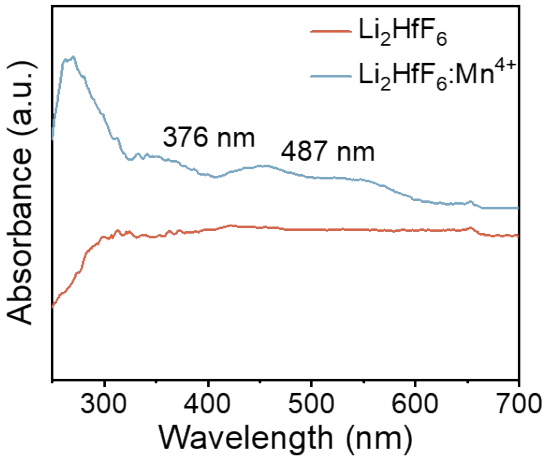

Figure S6. UV-vis absorption spectra of Li_2HfF_6 host and Li_2HfF_6:Mn^{4+} phosphor.

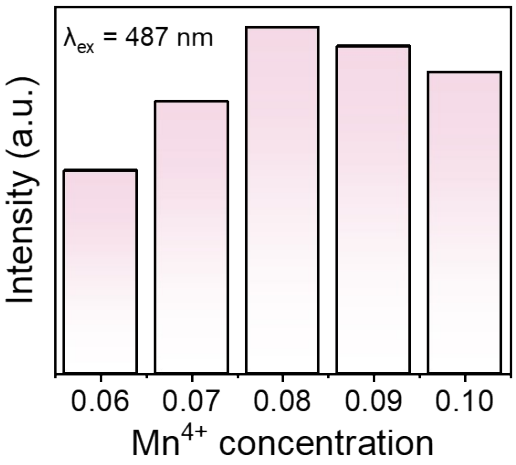

Figure S7. Comparison of luminescence intensity at 487 nm excitation wavelength for samples with different Mn^{4+} doping concentrations (0.06-0.10).

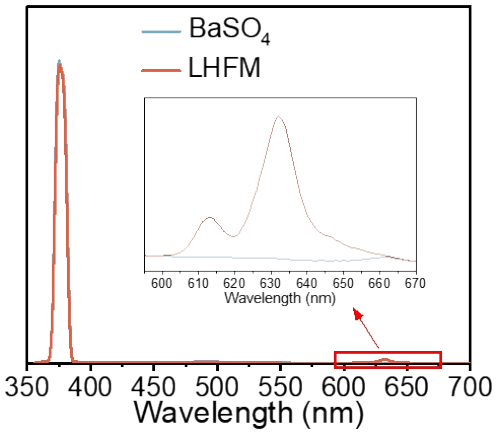

Figure S8. Quantum efficiency spectrum of LHFM.

The quantum efficiency measurements were carried out using an Edinburgh FS5 fluorescence spectrometer equipped with an integrating sphere, where $BaSO_4$ was employed as the blank reference for baseline calibration. The absorption efficiency (AE), internal quantum efficiency (IQE), and external quantum efficiency (EQE) were calculated according to the following equations:

$$AE = \frac{\int \lambda[E(\lambda) - R(\lambda)]d\lambda}{\int \lambda E(\lambda)d\lambda} \quad \text{(S1)}$$

$$IQE = \frac{\int \lambda P(\lambda)d\lambda}{\int \lambda E(\lambda)d\lambda} \quad \text{(S2)}$$

$$EQE = IQE \times AE = \frac{\int \lambda P(\lambda)d\lambda}{\int \lambda E(\lambda)d\lambda} \quad \text{(S3)}$$

where $E(\lambda)/h\nu$, $R(\lambda)/h\nu$, and $P(\lambda)/h\nu$ represent the numbers of photons in the excitation, reflectance, and emission spectra, respectively. Based on these calculations, the IQE of LHFM was determined to be 55.5%, while the absorption efficiency was measured to be 3.89%, corresponding to an EQE of 2.16%. It should be noted that the relatively low EQE mainly originates from the weak absorption characteristic of the spin-forbidden d-d transitions of Mn^{4+} ions in fluoride hosts, which limits the overall photon harvesting efficiency.

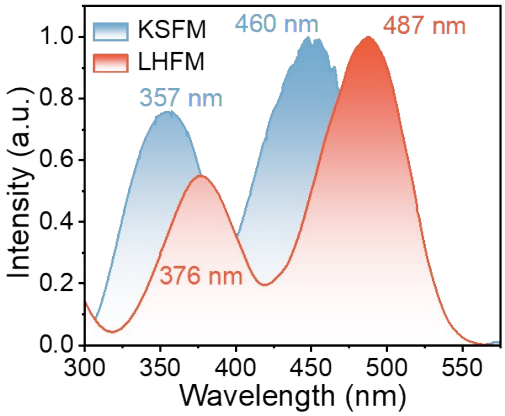

Figure S9. Comparison of excitation peak normalization between LHFM and KSFM.

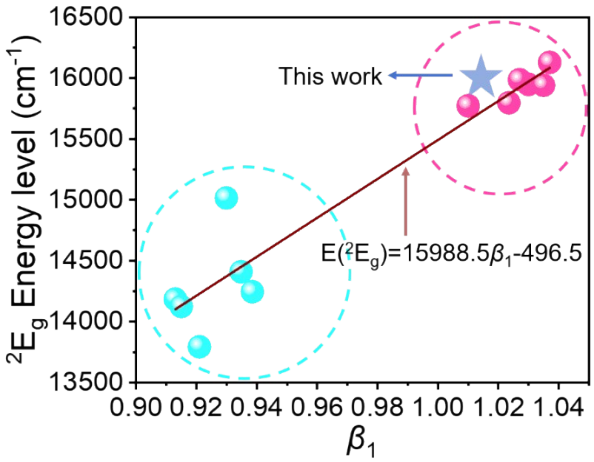

Figure S10. Linear energy relationship between $^2E_g \rightarrow {}^4A_{2g}$ of octahedral center Mn^{4+} and β_1.

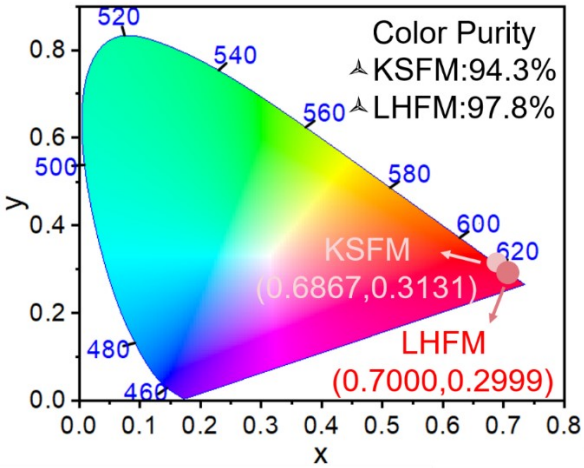

Figure S11. CIE chromaticity diagrams of LHFM and KSFM.

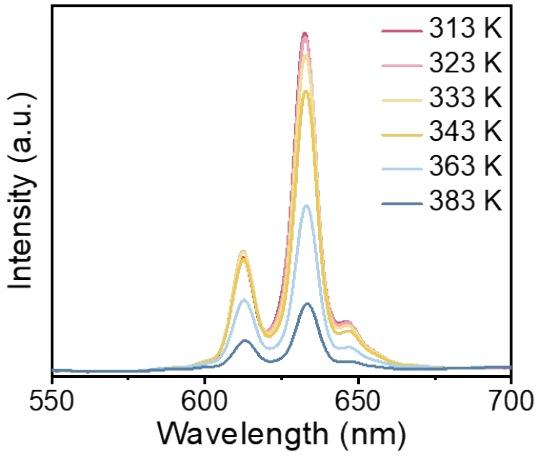

Figure S12. Thermal stability spectrum of LHFM.

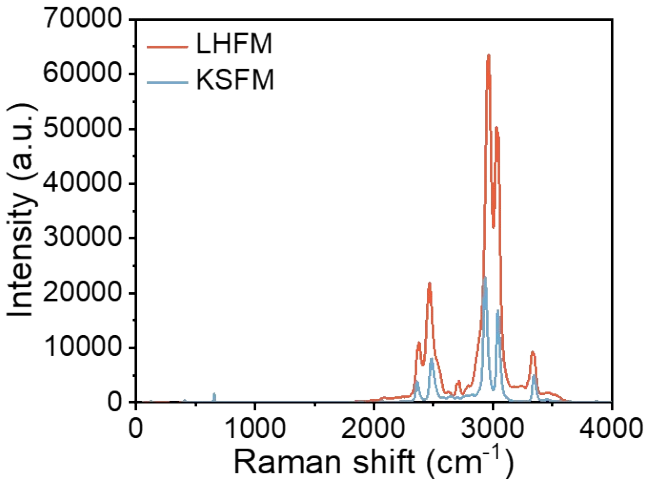

Figure S13. Raman comparison diagrams of LHFM and KSFM.

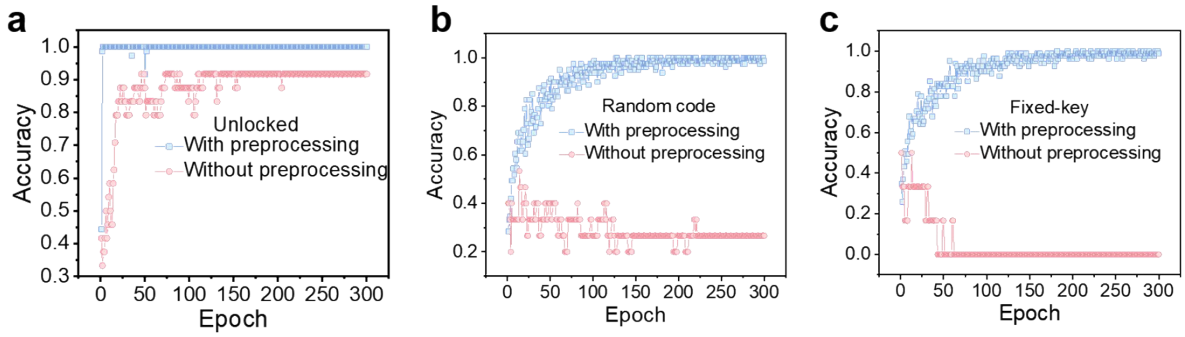

Figure S14. Recognition accuracy under different conditions as a function of training time.

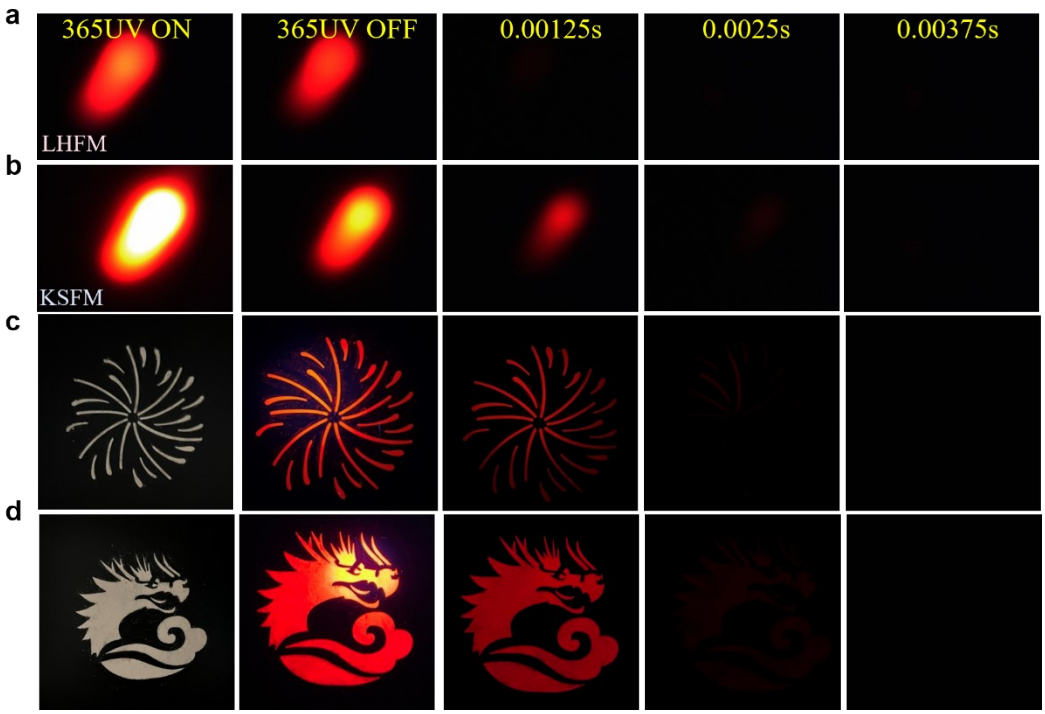

Figure S15. Color comparison of LHFM and KSFM as a function of decay time.

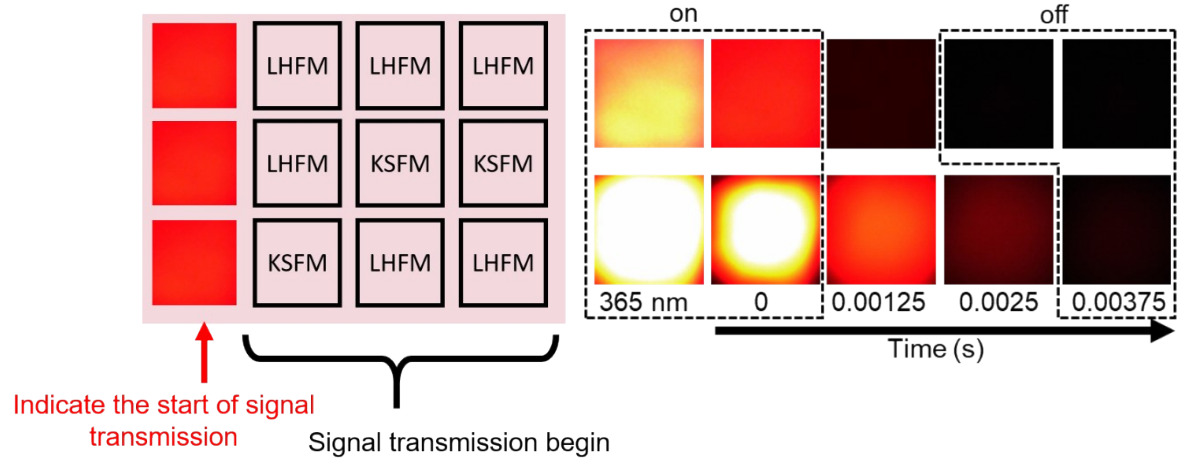

Figure S16. Anti-counterfeiting application of LHFM.

Table S1.

Refined crystallographic data of Li_2HfF_6:xMn^{4+}(x = 0.06-0.10).

Chemical formula	Li_2HfF_6:0.06Mn^{4+}	Li_2HfF_6:0.07Mn^{4+}	Li_2HfF_6:0.08Mn^{4+}	Li_2HfF_6:0.09Mn^{4+}	Li_2HfF_6:0.10Mn^{4+}
Space group	*P*-31*m*	*P*-31*m*	*P*-31*m*	*P*-31*m*	*P*-31*m*
a (Å)	4.96951	4.96937	4.96894	4.96902	4.9688
b (Å)	4.96951	4.96937	4.96894	4.96902	4.9688
c (Å)	4.64276	4.64289	4.6429	4.64191	4.64156
α (deg)	90	90	90	90	90
β (deg)	90	90	90	90	90
γ (deg)	120	120	120	120	120
V (Å^3)	99.29647	99.29375	99.27693	99.2586	99.24243
R_{wp}	8.81%	7.52%	8.74%	9.14%	8.62%
R_p	8.42%	7.62%	7.42%	9.14%	7.74%
χ^2	1.113	0.992	1.499	1.156	1.398

Table S2.
Spectroscopic parameters and β_1 values of Mn^{4+} ions for as-reported Mn^{4+}-activated fluorides and oxides phosphor reported by other literature.

Phosphors	Dq/cm^{-1}	B/cm^{-1}	C/cm^{-1}	β_1	$E(^2E_g)$ /cm^{-1}	Refs.
Na_2TiF_6	2100	504	4052	1.037	16129	1
K_2XF_7(X = Ta,Nb)	2166	511	3955	1.03	15948	2
$KZnF_7$	2105	607	3785	1.0235	15797	3
$(NH_4)_2NaInF_6$	2144	531	3874	1.01	15772	4
$K_3MoO_3F_3$	2127.7	575.43	3873	1.027	15986.3	5
$K_2Na(MoO_2F_4)_2{\cdot}H_2O$	2128	484	4075	1.035	15940	6
$KGaP_2O_7$	2204	782	2804	0.9385	14245	7
$SrGd_2Al_2O_7$	2053	767	2762	0.921	13793	8
Gd_2ZnTiO_6	1980	639	3132	0.913	14184	9
$Li_3Mg_2SbO_6$	2096	812	2634	0.9299	15015	10
$La(MgTi)_{1/2}O_3$	2053	700	2959	0.915	14124	11
Sr_2LaNbO_6	2101	722	3001	0.9348	14409	12
Li_2HfF_6	**2053.38**	**563.65**	**3092.5**	**1.01**	**15797.79**	**This work**

Table S3.
KSFM and LHFM attenuation fitting parameters.

Parameter	LHFM	KSFM
A_1	0.2068	0.33448
τ_1 (μs)	896	9073
A_2	0.86994	0.60211
τ_2 (μs)	3032	9074

The fast and slow decay components can be attributed to two distinct relaxation pathways of Mn^{4+} within the coupled excited-state system. The slow component (τ_2) predominantly originates from the spin-forbidden $^2E_g \rightarrow {}^4A_{2g}$ transition, which is characteristic of Mn^{4+} in relatively symmetric octahedral environments and is associated with a low radiative transition probability. In contrast, the fast component (τ_1) mainly arises from a coupling-assisted relaxation pathway involving the ^2E_g and $^4T_{2g}$ states. Thermally assisted interaction between these states facilitates population redistribution within the excited-state manifold, effectively increasing the contribution of states with higher radiative transition probability and resulting in a shortened decay component.

References

1. Y. Liu, T. Wang, Z. Tan, J. Meng, W. Huang, Y. Huang, S. Liao and H. Zhang, *Ceram. Int.*, 2019, **45**, 6243-6249.
2. H. Lin, T. Hu, Q. Huang, Y. Cheng, B. Wang, J. Xu, J. Wang and Y. Wang, *Laser Photonics Rev.*, 2017, **11**, 1700148.
3. T. Hu, H. Lin, F. Lin, Y. Gao, Y. Cheng, J. Xu and Y. Wang, *J. Mater. Chem. C*, 2018, **6**, 10845-10854.
4. H. Wang, X. Liu, F. Hong, Y. Dong, Y. Li, G. Liu, J. Wang, D. Li, W. Yu and X. Dong, *J. Lumin.*, 2022, **251**, 119242.
5. J. Zhang, Q. He, D. Gao, M. Liu, J. Peng and X. Ye, *J. Mol. Struct.*, 2025, **1338**, 142317.
6. Q. Qu, H. Zhang and H. Ji, *J. Mater. Chem. C*, 2024, **12**, 5488-5495.
7. N. V. Naresh and N. Lee, *J. Lumin.*, 2019, **214**, 116565.
8. J. Xiao, J. Zhang, C. Tu, J. Liao, H. Wen and G. Gong, *Opt. Mater.*, 2021, **118**, 111219.
9. H. Chen, H. Lin, Q. Huang, F. Huang, J. Xu, B. Wang, Z. Lin, J. Zhou and Y. Wang, *J. Mater. Chem. C*, 2016, **4**, 2374-2381.
10. J. Zhong, X. Chen, D. Chen, M. Liu, Y. Zhu, X. Li and Z. Ji, *J. Alloys Compd.*, 2019, **773**, 413-422.
11. Z. Zhou, J. Zheng, R. Shi, N. Zhang, J. Chen, R. Zhang, H. Suo, E. M. Goldys and C. Guo, *ACS Appl. Mater. Interfaces*, 2017, **9**, 6177-6185.
12. A. Fu, A. Guan, D. Yu, S. Xia, F. Gao, X. Zhang, L. Zhou, Y. Li and R. Li, *Mater. Res. Bull.*, 2017, **88**, 258-265.